energies

MDPI

Article

Concept and Numerical Analysis of a Vehicle-Motion Energy Harvesting Turbine Integrated with a Noise Barrier

Paweł Ligęza [1,*], Michał Przepiórski [2] and Hubert Jabłoński [1]

[1] The Strata Mechanics Research Institute of the Polish Academy of Sciences, Reymonta 27, 30-059 Cracow, Poland; hubert.jablonski@imgpan.pl
[2] Department of Fundamental Research in Energy Engineering, Faculty of Energy and Fuels, AGH University of Krakow, Mickiewicza 30, 30-059 Cracow, Poland; przepiordok@agh.edu.pl
* Correspondence: ligeza@imgpan.pl

Abstract

The paper presents the concept of a turbine-based energy harvester designed to recover kinetic energy from airflow generated by a moving vehicle and integrated with a roadside acoustic barrier. The proposed solutions employ a vertical-axis aerodynamic turbine positioned within a cavity in the barrier and various airflow guiding structures intended to enhance the efficiency of energy transfer from turbulent airflow to the turbine rotor. To evaluate the effectiveness of the proposed concepts, two-dimensional CFD simulations were conducted in the ANSYS Fluent environment using the k–ε turbulence model. Three airflow deflector geometries and one reference configuration without a deflector were analyzed. The performance of each configuration was assessed based on the maximum instantaneous power and the average power generated by the turbine during a single vehicle pass-by event. The results demonstrated a significant influence of the airflow guide geometry on system performance. The most effective configuration achieved an average power output of approximately 7 W during a single vehicle pass-by event, whereas the configuration without an airflow guide exhibited significantly lower energy recovery efficiency. The obtained findings confirm the potential of the analyzed technology as a power source for autonomous low-power roadside infrastructure systems.

Keywords: energy harvesting; turbine; CFD; flow deflector

1. Introduction

The need to provide energy to meet humanity's ever-increasing civilizational needs is one of the key challenges of the 21st century. The planet's population exceeds eight billion [1], and the average daily electricity demand per person currently stands at 10 kWh [2]. The use of fossil fuels in energy production and the associated greenhouse gas emissions may be one of the causes of the increase in average atmospheric temperature, negatively impacting the course of many phenomena [3–5]. Natural disasters, such as large-scale forest fires, are increasing, emitting enormous amounts of carbon dioxide into the atmosphere [6]. Economic, social, and political factors are leading to mass migration, social unrest, and wars, making the global energy system unstable and unpredictable [7].

The above factors are leading to changes in the energy industry, including the large-scale development of renewable energy, primarily based on wind turbines and photovoltaic farms. Renewable energy utilizes the Sun as a primary, inexhaustible, on a human time scale, energy source. This technology reduces greenhouse gas emissions, and the energy

Academic Editors: Kwok Tong Chau and Lars Johanning

Received: 5 May 2026
Revised: 13 June 2026
Accepted: 30 June 2026
Published: 2 July 2026

sources are distributed [8]. In addition to generating electricity, solar energy is also used to heat water and air for utilitarian purposes. Article [9] presents a review of solar air heater solutions and analyzes the current state of development of SAH collectors with baffles. It was found that increasing air velocity and turbulence in the channels, improving the baffle position, and introducing perforations to suppress vortices improve heat transfer efficiency and reduce pressure losses by over 40%. Direct solar heat utilization technologies reduce the use of electricity for heating purposes.

Energy harvesting technology also contributes, on a small but constantly growing scale, to the rational management of energy processes. Energy harvesting is the process of obtaining a useful form of energy, primarily electric current, from natural and anthropogenic sources, whose energy is usually dissipated into the environment under normal conditions [10]. The harvesting process generally produces small amounts of electric current, which are used to power local devices. The primary energy sources in the harvesting process are mechanical, thermal, and electromagnetic energy [11]. Mechanical energy is converted into electric current using electromagnetic [12,13], piezoelectric [14,15], and increasingly triboelectric [16,17] phenomena. A hybrid combination of the above methods for converting mechanical energy into electrical energy is also used. In [18], a combination of piezoelectric and triboelectric processing was proposed, and the system was equipped with a synergistic mechanism based on the evolution of dynamic control. This resulted in higher harvester efficiency. Another important development direction is mechanical, intelligent energy harvesting [19], in which the system identifies its own state and external impact and actively responds to these conditions. Harvesters that convert mechanical energy into electricity are becoming increasingly complex systems, and thanks to the use of adaptive mechanisms [20], their efficiency is constantly improved.

Thermoelectric [21,22] and pyroelectric [23,24] conversion methods are used to convert thermal energy. Electromagnetic energy, depending on the frequency, is processed in photovoltaic panels [25,26] or in antenna systems [27,28].

An interesting field for the application of energy harvesting methods is transportation routes: roads, highways, railways, and waterways [29]. These areas are easily accessible, occupy vast areas, and constitute largely exposed flat surfaces. At the same time, transportation infrastructure requires power sources for signaling and information systems, lighting, monitoring, traffic control, toll collection, and data transmission. The primary energy sources in the harvesting process are primarily moving vehicles. Other primary energy sources include wind [30], solar radiation [31], heat accumulated in surfaces and geothermal sources [32], and electromagnetic radio waves [33].

The mechanical energy of vehicle movement can be transferred to harvesters in two ways: directly via the contact method and through the air surrounding the vehicles. Contact methods are primarily based on the use of speed bumps, whose movement, under the pressure of the vehicle, is converted into electrical energy using mechanical systems cooperating with mechanical-electrical converters [34–36]. In addition to speed bumps, systems using vehicle pressure on the road surface [37] and sliding plates [38] have been developed. These methods have a significant application area and are the subject of research and implementation in many research centers.

The energy of vehicles traveling on roads is transferred to the surrounding air primarily in the form of kinetic energy, setting the air in motion. A small portion of the vehicle energy is also emitted in the form of heat and acoustic waves [39], which constitute environmentally harmful noise. The heat is dissipated in the atmosphere, and in practice, this energy cannot be effectively recovered. However, attempts are being made to recover some of the energy from acoustic waves. A review of technologies used to recover useful energy from acoustic waves generated by vehicles is included in article [40]. This technology uses acoustic-

electric transducers, resonators, and array systems typically placed in acoustic screens and other flat surfaces of road infrastructure. The authors emphasize that there is a high barrier between laboratory research and potential practical application. Despite this, they consider this energy harvesting method intriguing. However, the current energy efficiency to cost ratio is negligible; the developed systems discussed in article [40] deliver power levels no higher than a few milliwatts.

Vehicles traveling at high speeds use most of their engine power to overcome air resistance, causing air movement that has a complex, turbulent nature [41–43]. Under normal conditions, this energy is dissipated, but harnessing this energy has significant potential and poses a challenge for scientists developing energy harvesting methods. The main stream of work in this area concerns the placement of vertical turbine assemblies within traffic routes, powered by air movement generated by passing vehicles. The turbines' rotational motion is typically converted into electricity in efficient electromagnetic generators. Other energy conversion methods are used much less frequently. The number of scientific publications in recent years on this topic is relatively small.

In article [44], the authors presented the results of simulation studies of the impact of a passing vehicle on a single, multi-blade vertical turbine placed by the road. The study analyzed the effect of vehicle speed and the distance between the vehicle and the turbine on the energy efficiency of a harvester. For the assumed simulation conditions, the maximum energy transferred to the turbine during a single vehicle pass was calculated at approximately 100 J. A review article [45] presents the directions of work of various research teams in this field. It discusses the types and shapes of turbines used in previous research and prototype designs, the issues of modeling the process of energy transfer from vehicle to turbine, and an original example of a harvester using vibrating leaf-shaped aerodynamic airfoils instead of a turbine. Article [46] presents the results of testing a two-blade vertical turbine designed for placement on a highway median. Experimental studies achieved a maximum instantaneous power output of approximately 700 mW.

The application of the triboelectric conversion method to a series of low-rise vertical turbines placed on a road is discussed in article [47]. The turbines are constructed as a vertical, rotating, outer cylinder with five aerodynamic blades. Inside the cylinder is a second, stationary cylinder of smaller diameter, with elastic sliding elements on its surface. These elements collect electric charges during the rotation of the outer cylinder. In tests on a single prototype, the energy parameters of this process were measured. The maximum output power was below 100 microwatts. The project of using turbines placed in a highway median between carriageways to power an electric vehicle charging station is analyzed in article [48]. The authors used computer simulation to optimize the turbine shape. The article also presents the design of a prototype vertical-axis turbine with two blades. The turbine is equipped with an electromagnetic generator with a maximum power of 45 W. However, the results of testing the prototype under real-world conditions are not presented, so the power generated by this harvester is unknown.

In this article, the authors analyze the innovative concept of placing energy harvester turbines within the recesses of noise barriers or other similar structures located along traffic routes. Additionally, in the proposed solution, air is directed onto the turbine blades using appropriately shaped guide vanes. This solution aims to increase the energy efficiency of turbine energy harvesters compared to harvesters placed in open spaces.

In Section 1, we present an introduction to the issue of energy harvesting on traffic routes and a brief overview of the state of the art in the field. Section 2 discusses the original concept of a turbine energy harvester integrated with a noise barrier or other roadside structure. Section 3 presents the results of simulation tests of the harvester for several

selected configurations. Section 4 discusses the conclusions from the research and the concept for further research.

2. Concept of a Turbine-Based Energy Harvester Integrated with a Noise Barrier

In the majority of vehicle-induced airflow energy harvesters described in the literature, aerodynamic turbines are installed near the roadway in open space [38–42]. A disadvantage of this arrangement is that only a small portion of the kinetic energy of the airflow is converted into useful energy. This is due to the fact that airflow generated by passing vehicles is multidirectional and turbulent in nature, and only a fractional portion of the air momentum is effectively transferred to the turbine.

The authors of the present study propose a novel harvester concept in which the turbine is integrated with a noise barrier or another similar structure forming a vertical surface located adjacent to a transportation route. Additionally, it is proposed to place an appropriately shaped aerodynamic guide vane between the vehicle and the turbine in order to redirect the airflow and thereby enhance harvester efficiency. The conceptual design of the proposed harvester is presented in Figure 1.

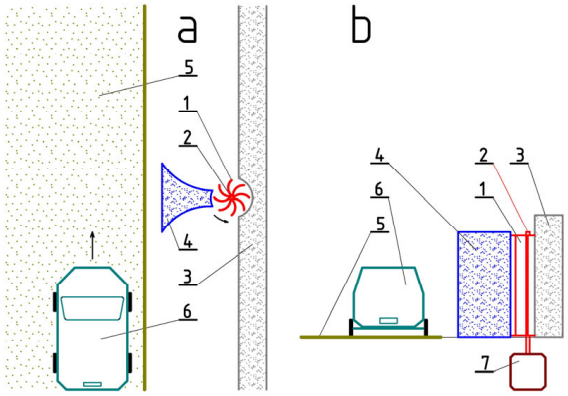

Figure 1. Concept of a vehicle-motion energy harvester: (**a**) top view; (**b**) rear view of the vehicle. 1—vertical-axis turbine, 2—turbine shaft, 3—noise barrier, 4—airflow guide vane, 5—roadway, 6—vehicle, 7—electromagnetic generator.

The proposed vehicle-motion energy harvester integrated with a roadside noise barrier or another wall-type structure located adjacent to the roadway consists of a vertical-axis aerodynamic turbine partially embedded within a recess in the noise barrier. The recess has the form of a cylindrical segment matched to the outer contour of the turbine. The turbine is composed of aerodynamic blades mounted on a vertical rotational shaft. This shaft is connected directly, or through a mechanical transmission system, to the rotor shaft of an electromagnetic electric generator. Between the roadway and the turbine, a column-shaped airflow guide vane is positioned to direct the airflow toward the turbine and to separate the incoming and outgoing air streams. On the roadway-facing side, the guide vane features an approximately flat surface. On the side facing the approaching vehicle, the vane has a concave surface designed to direct the incoming airflow toward the turbine through an inlet gap located between the vane and the barrier. On the turbine-facing side, the vane surface has the form of a cylindrical segment matched to the outer contour of the turbine. On the downstream side, corresponding to the vehicle moving away from the harvester, the column incorporates a concave surface that directs the air exiting the turbine through an outlet gap located between the vane and the barrier, back toward the roadway.

As a vehicle approaches the harvester, it pushes air ahead of itself, which is redirected by the guide vane toward the concave side of the turbine blades, creating a region of

elevated pressure upstream of the turbine. After passing the harvester, the vehicle generates a low-pressure region behind the guide vane, thereby drawing air out of the turbine. This induces rotational motion of the turbine, and the electromagnetic generator coupled to the turbine shaft produces electrical power, which may be stored and subsequently used, for example, to supply roadway signaling, monitoring, and traffic control systems. It is possible to deploy multiple energy harvesting units at intervals along the noise barrier and aggregate their output in order to increase both the total harvested energy and the continuity of power generation. The proposed harvester design aims to improve the utilization efficiency of the kinetic energy contained in vehicle-induced airflow compared with free-standing turbine configurations. In the proposed arrangement, the incoming and outgoing airflow streams are separated, a pressure gradient is generated across the turbine, and the turbine is partially shielded from airflow components that would otherwise oppose its rotational motion, thereby enhancing the overall energy conversion efficiency of the device.

Figure 1 presents the general concept of the proposed vehicle-motion energy harvester. Various design modifications are possible, including optimization of the airflow guide vane geometry and structure, increasing the number of guide vanes, altering the turbine rotation direction, or employing alternative turbine types. In the initial stage of the proposed harvester development, numerical simulations were conducted for several selected configuration variants.

3. Analysis of Selected Design Variants

To evaluate the influence of airflow guide vanes on the performance of roadside energy harvesting systems, numerical analyses were conducted using the ANSYS Fluent 2024 R2 computational environment, license server 1055@ansys.licencja.icm.edu.pl.

The following hardware parameters were used for the calculations: Intel Core i5-7500 CPU 3.40 GHz (3.41 GHz), 32 GB of installed RAM and an NVIDIA Quadro K620 2 GB graphics card. Each simulation took approximately 11 h, utilizing all 4 processor cores. The approximate CPU time of each simulation was 44 core-hours.

The research plan involved performing a series of numerical simulations aimed at determining how different airflow-guiding configurations affect the power generated by a roadside turbine. An additional important objective was to establish a baseline reference value for the energy recovered by the turbine operating without any diffuser or flow-guiding structure positioned upstream.

3.1. Geometry

To model the complete process involving vehicle passage in the vicinity of the turbine under conditions characterized by the presence of developed wake structures behind the vehicle—including the high-pressure zone ahead of the vehicle and the low-pressure wake region behind it—as well as the turbine response to the resulting pressure variations, a two-dimensional geometry was created. The computational domain comprised a section of roadway with a turbine positioned at the roadside, together with a centrally located vehicle model. A complete view of the analyzed geometry is presented in Figure 2.

The characteristic dimensions of the geometry are listed in Table 1. These parameters remained unchanged in all simulations.

In the successive simulations, different geometric variants of the deflector located between the vehicle and the turbine were investigated. Consequently, the geometry of the airflow guide vane differed in each simulation case. The geometries of this particularly significant region for the four analyzed simulation variants are presented in Figure 3.

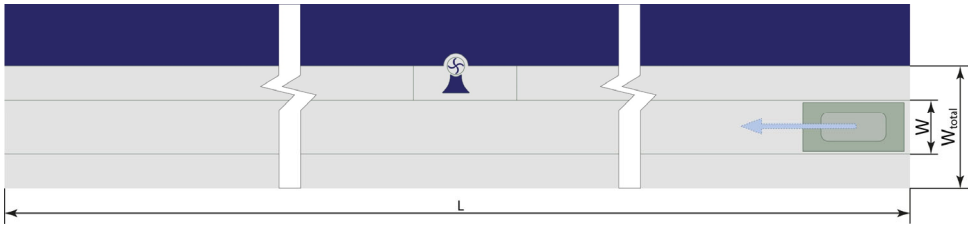

Figure 2. Geometry of the analyzed case. The arrow indicates the direction of vehicle motion.

Table 1. Constant geometric dimensions.

Parameter	Value
Geometry length (L)	250 [m]
Lane width (W)	3.75 [m]
Total geometry width (W_{total})	8.48 [m]
Turbine circle diameter	1.2 [m]
Vehicle model length and width	4.5 × 2 [m]
Overset mesh domain length and width	7 × 3.4 [m]
Gap between vehicle and deflector	1.375 [m]
Distance between turbine and deflector	0.125 [m]
Blade length	0.5 [m]
Blade setting angle	120 [°]

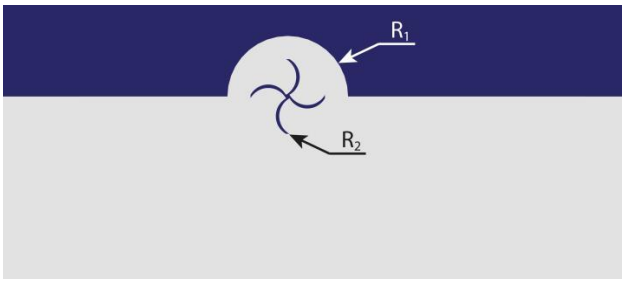

(**a**)

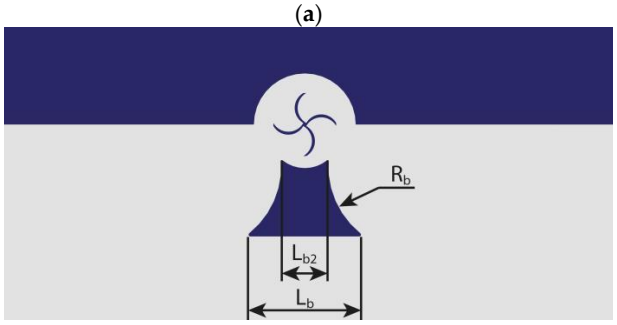

(**b**)

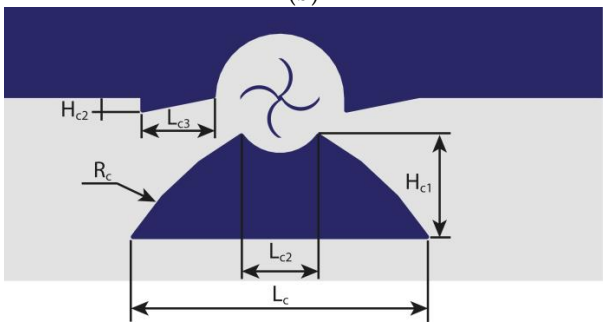

(**c**)

Figure 3. *Cont.*

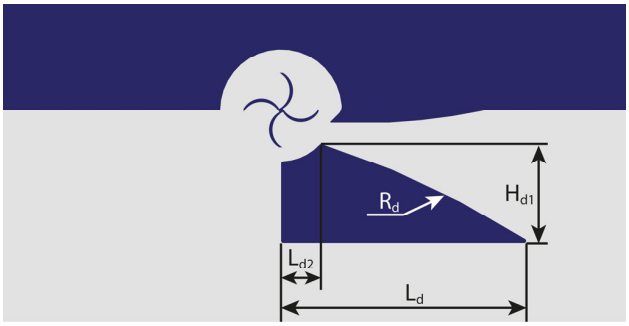

(**d**)

Figure 3. Geometry of airflow guide vane configurations used in individual simulations: (**a**) no deflector; (**b**) symmetric deflector promoting rapid boundary layer separation; (**c**) symmetric deflector promoting gradual boundary layer separation; (**d**) asymmetric deflector.

The geometry shown in Figure 3a does not include a deflector. The designations shown in the figure remain constant for all simulations: R_1 denotes the radius of the semicircular cavity in the acoustic barrier (0.85 m), while R_2 represents the curvature radius of the turbine blade (0.29 m). Figure 3b presents a symmetric deflector designed to promote rapid boundary layer separation and thereby enhance momentum transfer to the turbine blades. The base length (L_b) of the deflector in configuration 3b is 2 m, and its side walls are concave at an angle of 55° (R_b). The deflector length in the immediate vicinity of the turbine (L_{b2}) is equal to 0.77 m. The deflector shown in Figure 3c is also symmetric; however, this concept assumes a more gradual boundary layer separation from its surface, while additional guide vanes mounted on the acoustic barrier are intended to intensify the airflow impact on the turbine blades. The base length of the deflector in configuration 3c is 4 m (L_c), its side walls are convex at an angle of 30° (R_c), the deflector width (H_{c1}) is 1.4 m, and the distance near the turbine (L_{c2}) is 1 m and the additional protrusions mounted on the barrier have a length of 1 m (L_{c3}) and a height of 0.2 m (H_{c2}), respectively. The only asymmetric deflector analyzed is presented in Figure 3d. In this concept, the structures located upstream of the turbine are intended to direct the airflow toward the turbine blades, while the absence of downstream obstacles allows utilization of the low-pressure wake region trailing the vehicle. The base length (L_d) of this deflector is 3.5 m, the deflector width (H_{d1}) is 1.4 m, whereas the deflector length in the turbine region (L_{d2}) is equal to 0.55 m, its side wall is convex at an angle of 15° (R_d), and the protrusion mounted on the acoustic barrier has a length of 2 m and a height of 0.2 m.

3.2. CFD Model

For the numerical analyses, the realizable k–ε turbulence model with enhanced wall treatment was selected. This is a fundamental two-equation numerical model belonging to the Reynolds-Averaged Navier–Stokes (RANS) family, while the enhanced wall treatment option improves solution accuracy in near-wall regions. The governing equations used to determine the turbulent kinetic energy and its dissipation rate in the k–ε model are presented as Equation (1) and Equation (2), respectively [49,50].

$$\frac{\partial}{\partial x_j}\cdot\left[\left(\mu+\frac{\mu_t}{\sigma_k}\right)\frac{\partial k}{\partial x_j}\right]+G_k+G_b-\rho\varepsilon-Y_M+S_K-\frac{\partial(\rho k)}{\partial t}-\frac{\partial\left(\rho k u_j\right)}{\partial x_j}=0 \quad (1)$$

where G_k—generation of turbulence kinetic energy due to mean velocity gradients [W/m^3], G_b—generation of turbulence kinetic energy due to buoyancy effects [W/m^3], k—turbulent kinetic energy [m^2/s^2], S_K—user-defined source term for the turbulence kinetic energy equation [W/m^3], t—time [s], u_i—velocity [m/s], x_j—Cartesian spatial coordinates [m],

Y_M—contribution of fluctuating dilatation in compressible turbulence to the overall dissipation rate [W/m^3], ε—dissipation rate [m^2/s^3], μ—molecular dynamic viscosity [Pa·s], μ_t—turbulent dynamic viscosity [Pa·s], σ_k—turbulent Prandtl number [-], ρ—density [kg/m^3].

$$\frac{\partial}{\partial x_j}\cdot\left[\left(\mu+\frac{\mu_t}{\sigma_\varepsilon}\right)\frac{\partial \varepsilon}{\partial x_j}\right]+\rho C_1 S_\varepsilon-\rho C_2\frac{\varepsilon^2}{k+\sqrt{v\varepsilon}}+C_{1\varepsilon}\frac{\varepsilon}{k}C_{3\varepsilon}G_b+S_\varepsilon-\frac{\partial(\rho\varepsilon)}{\partial t}-\frac{\partial(\rho\varepsilon u_j)}{\partial x_j}=0 \quad (2)$$

where C_1—variable coefficient of the realizable k–ε turbulence model [-], $C_{1\varepsilon}$, $C_{2\varepsilon}$, $C_{3\varepsilon}$—constants for the model [-], S_ε—user-defined source term for the turbulence dissipation rate equation [$kg/m{\cdot}s^4$], v—kinematic viscosity [m^2/s], σ_ε—turbulent Prandtl number for ε [-].

Since buoyancy and compressibility effects were neglected, the terms G_b and Y_M were set to zero in the present simulations.

3.3. Computational Mesh

Prior to generating the final computational mesh, one of the key stages of the CFD modeling procedure involved performing the necessary mesh sensitivity tests to evaluate the influence of the number of mesh elements on the simulation results. The test was based on a comparison of the torque parameter, following methodologies reported in previous studies on similar topics [51–53].

The mesh sensitivity analysis was performed for the airflow guide vane configuration presented in Figure 3b. The numerical parameters of the individual meshes are summarized in Table 2.

Table 2. Parameters of the numerical meshes used during the mesh sensitivity analysis.

Mesh No.	Number of Elements	Maximum Torque [N·m]	Minimum Torque [N·m]	CPU Time [Hours; Core-Hours]
Mesh 1	247,315	8.651	−4.443	7; 28
Mesh 2	410,866	8.432	−3.426	11; 44
Mesh 3	606,517	8.284	−3.379	17; 68
Mesh 4	819,033	8.487	−3.578	23; 92

A graphical representation of the mesh sensitivity test results was also provided. Figure 4 presents the turbine torque values obtained for each simulation as a function of consecutive time steps.

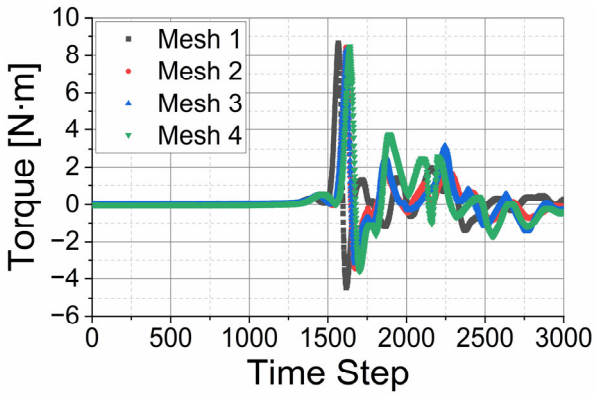

Figure 4. Turbine torque values as a function of time step for the analyzed numerical meshes.

Based on the obtained results, the final numerical simulations were performed using mesh number 2. The results obtained with this mesh do not differ significantly from those achieved with finer meshes (0.2% for maximum torque and 5.2% for minimum torque compared to mesh number 4). In addition, the waveform presented in Figure 4 exhibits a similar trend, while the computational time required for a single simulation case is more than two times shorter. Therefore, mesh number 2 was considered an appropriate compromise between computational cost and solution accuracy.

The computational mesh was generated in the ANSYS Meshing module over the entire computational domain. Owing to the partially symmetric geometry of the model (excluding the vehicle and the region surrounding the turbine), the Sizing and Number of Divisions options were employed to discretize the domain efficiently. The region surrounding the airflow guide vane, as well as the interior of the turbine circular domain, was discretized using the Sizing function by specifying the target mesh element size. Separate mesh settings were applied to the overset mesh region and the vehicle model, where the Sizing option was likewise utilized. Additionally, smooth transition inflation layers were introduced in critical regions of the geometry, namely around the vehicle model, along the acoustic barrier walls, around the turbine blades, and adjacent to the deflector walls. Representative mesh distributions in the selected computational regions are shown in Figure 5.

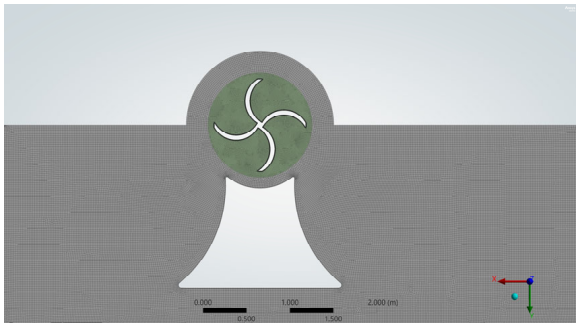

(**a**)

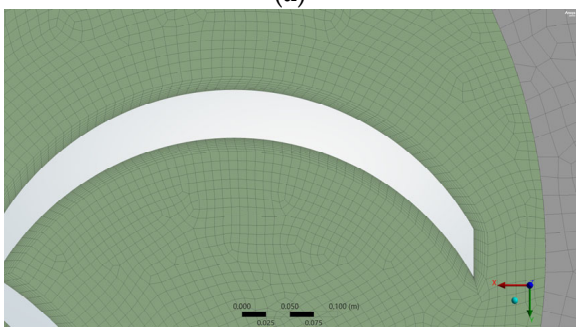

(**b**)

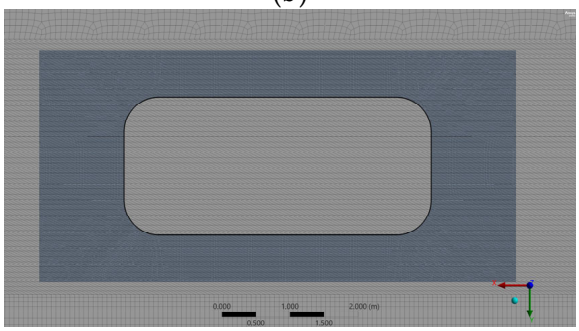

(**c**)

Figure 5. Example of computational mesh used in the simulations: (**a**) turbine and airflow guide vane region; (**b**) detailed mesh near the blade; (**c**) vehicle and overset mesh region.

As a consequence of performing four simulations with unique geometric configurations, the resulting computational meshes differed in both parameters and total element count. Every effort was made to maintain comparable computational accuracy and consistent meshing settings across corresponding regions of the geometry. The parameters of the individual meshes are summarized in Table 3. Based on these values, it can be concluded that the obtained mesh quality metrics satisfy the criteria required for considering the meshes numerically acceptable [54].

Table 3. Parameters of the computational meshes.

Mesh No.	Deflector Type (Figure 3)	Number of Elements	Maximum Skewness	Minimum Orthogonal Quality
1.	a	410,733	0.837	0.165
2.	b	410,866	0.822	0.166
3.	c	409,526	0.836	0.165
4.	d	409,713	0.821	0.165

Due to the dynamic nature of the simulations, requiring translational motion of the vehicle model and rotational motion of the turbine, appropriate dynamic mesh settings were applied. The moving vehicle model was placed within an overset mesh region, and its motion was implemented using a User-Defined Function (UDF). The rotating turbine was enclosed within a circular subdomain, at whose boundary unshared topology was defined, while mesh rotation was implemented using the Dynamic Mesh framework with the Six Degrees of Freedom (Six-DOF) option enabled. In this case, due to the two-dimensional nature of the simulation, the Six-DOF option utilizes only one of the six available degrees of freedom.

The UDF code used to simulate vehicle motion through the overset mesh was defined as follows:

```
#include “udf.h”
DEFINE_CG_MOTION(translational_profile, dt, vel, omega, time, dtime)
{
real u1 = 27.0;
vel [0] = u1;
vel [1] = 0.0;
vel [2] = 0.0;
}
```

The configuration of the Six-DOF method was initiated by enabling the “One DOF Rotation” option. Subsequently, additional Dynamic Mesh Zones were defined. The turbine blades, the region surrounding the turbine, and the contact region between the rotating geometry and the stationary domain were all defined as rigid bodies. Furthermore, the region around the turbine and the contact region were specified as passive zones, which was also enabled in the settings.

3.4. Boundary Conditions

The vehicle velocity was maintained constant at 27 m/s throughout the entire simulation. The vehicle moved from the right to the left side of the computational domain, passing the turbine on its right-hand side. The turbine moment of inertia was set to 0.05 kg·m^2. The simulations were performed using a transient solver formulation. The time step was set to 0.001 s, the total number of time steps was 2000, and the number of iterations per time step was set to 20.

The time step was selected so that the vehicle displacement during a single time step remained smaller than the characteristic cell size within the overset mesh region surrounding the vehicle. This criterion is associated with maintaining the local Courant number at or below unity, which is commonly used as a guideline for selecting an appropriate time step in transient CFD simulations and ensuring sufficient temporal resolution of the flow field. The applied criterion is described by Equation (3), from which Equation (4) is directly derived. Equation (5) presents the calculation of the time step used in the present study [55].

$$C = \frac{u \cdot \Delta t}{\Delta x} \leq 1 \tag{3}$$

$$\Delta t \leq \frac{\Delta x}{u} \tag{4}$$

where C—Courant number [-], u—vehicle velocity [m/s], Δt—time step [s], Δx—characteristic cell size within the overset mesh region surrounding the vehicle [m].

$$\Delta t = \frac{0.027}{27} = 0.001\ [s] \tag{5}$$

The selected time-step value is also consistent with available literature data and recommendations reported in similar studies [51,56,57].

3.5. Numerical Model Validation

The accuracy of the implemented numerical model, together with the adopted solver settings, was verified by comparing the simulation results obtained for a benchmark case with reference data available in the literature. For this purpose, the flow around a circular cylinder at a Reynolds number of 3900 was selected. This case represents a classical benchmark problem that has been extensively investigated both experimentally and numerically, providing a large amount of high-quality reference data.

Two parameters were selected for comparison: the mean drag coefficient and the Strouhal number. These parameters enable the assessment of the model's ability to reproduce the key characteristics of the flow field. The drag coefficient is one of the fundamental parameters describing the aerodynamic forces acting on a body immersed in a fluid flow. It is defined according to Equation (6) [58].

$$C_d = \frac{2F_d}{\rho u^2 A} \tag{6}$$

where A—reference area [m^2], F_d—drag coefficient [N], u—flow velocity [m/s], ρ—mass density of the fluid [kg/m^3].

The Strouhal number is one of the fundamental dimensionless parameters used to characterize unsteady flows, particularly when comparing cases with identical Reynolds numbers. In the present study, it was used to assess the vortex shedding frequency in the wake of the circular cylinder. The Strouhal number can be determined using Equation (7) [59].

$$St = \frac{f \cdot L}{u} \tag{7}$$

where f—dominant vortex shedding frequency [Hz], L—characteristic length [m], u—flow velocity [m/s].

The mean drag coefficient was calculated from the instantaneous values recorded at each time step using the Report Definitions function available in ANSYS Fluent. During post-processing, the initial transient portion of the simulation, corresponding to the startup phase before the establishment of a fully periodic unsteady flow, was excluded from the

analysis. The arithmetic mean was subsequently calculated from the remaining statistically stationary portion of the signal. The Strouhal number was determined through a frequency analysis of the lift force acting on the cylinder, which was also recorded using the Report Definitions function. The time-history signal was processed using the Fast Fourier Transform (FFT) tool implemented in ANSYS Fluent. The dominant oscillation frequency (f) was identified as the frequency corresponding to the global maximum of the amplitude spectrum.

The validation simulations were performed using the same solver settings as those applied in the main numerical model. The validation geometry was designed to ensure consistency with benchmark configurations reported in the literature and to maintain the Reynolds number corresponding to the selected reference case. Due to the complexity of the main numerical model, a two-stage validation procedure was adopted. In the first stage, a circular cylinder with a diameter (D) of 0.02 m was placed in a two-dimensional computational domain. The distance between the cylinder front surface and the inlet boundary (marked with blue arrows) was equal to 9D, while the distance between the cylinder rear surface and the pressure outlet boundary was equal to 30D. The distances between the upper and lower cylinder surfaces and the corresponding symmetry boundaries were both equal to 4.5D. In the second stage, the same cylinder was placed inside an overset mesh region with a length of 3D and a width of 2D. Schematics of both validation geometries are presented in Figure 6.

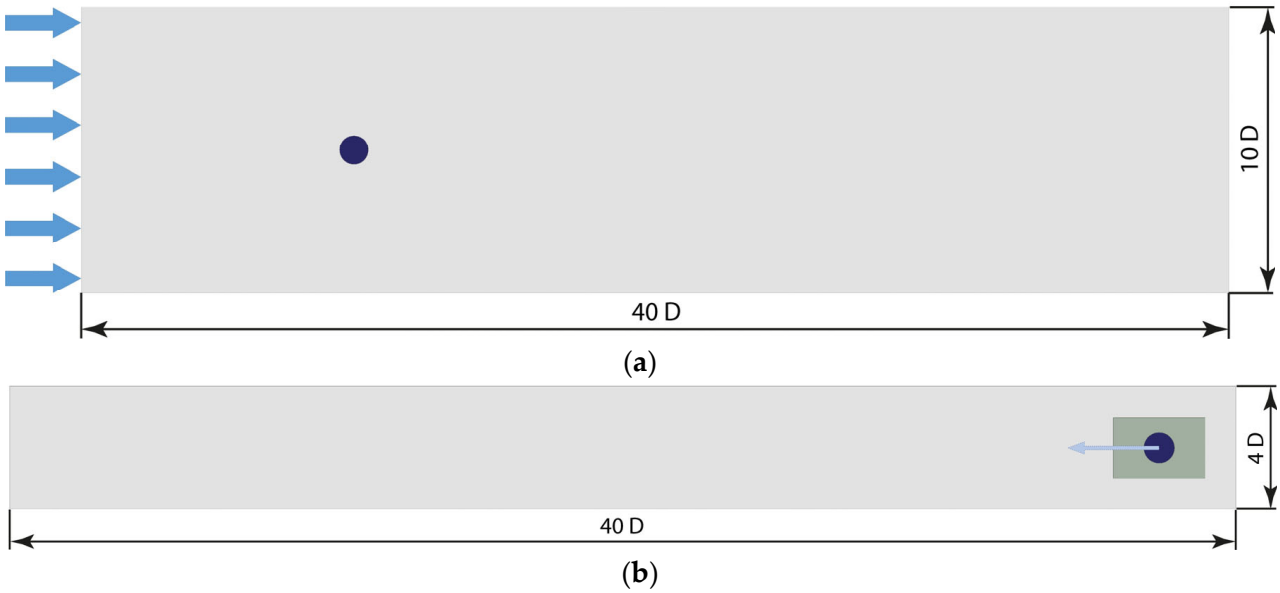

Figure 6. Geometry of the circular cylinder used for numerical model validation: (**a**) stationary-cylinder test; (**b**) overset mesh test.

The two-stage validation procedure was intended to demonstrate agreement between the predicted flow characteristics and the available reference data, as well as to verify that the application of the overset mesh technique does not introduce significant discrepancies in comparison with the stationary mesh solution.

The numerical simulations produced the flow field presented in Figure 7. A well-developed von Kármán vortex street was observed downstream of the cylinder, generated by the alternating shedding of vortices from the upper and lower sides of the cylinder.

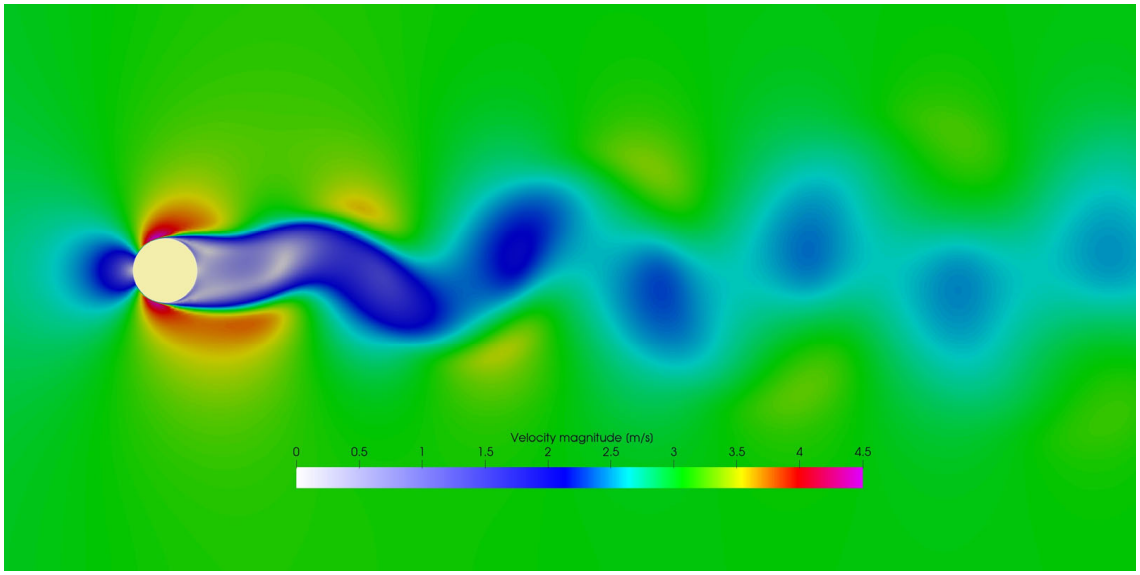

Figure 7. Instantaneous velocity magnitude field showing the von Kármán vortex street formed downstream of the circular cylinder.

A key aspect of the numerical model validation is the comparison of the mean drag coefficient and Strouhal number with reference data available in the literature. The mean drag coefficient was determined by averaging its time history after the flow reached a statistically stationary periodic regime characterized by the formation of a von Kármán vortex street. A comparison of the obtained numerical results with literature data is presented in Table 4 [60–66].

Table 4. List of literature parameters and own analyses for the tested cylinder.

Author	Type of Analysis	Reynolds Number	Strouhal Number	Mean Drag Coefficient
Parnaudeau et al. [60]	Experimental—HWA	3900	0.208 ± 0.002	-
Kravchenko et al. [61]	Experimental—PIV	3900	0.215 ± 0.005	0.99 ± 0.05
Lysenko et al. [62]	CFD—LES	3900	0.210	0.97
Ouvrard et al. [63]	CFD—LES	3900	0.220	0.94
Lourenco [64]	Experimental—PIV	3900	0.220	0.99
Mani et al. [65]	CFD—LES	3900	0.210	0.99
Franke and Frank [66]	CFD—LES	3900	0.210	0.99
Stationary-cylinder test	CFD—k–ε	3900	0.203	0.94
Overset mesh test	CFD—k–ε	3900	0.205	0.97

The results presented in Table 4 demonstrate good agreement between the numerical predictions and the available reference data. The obtained Strouhal numbers (0.203 and 0.205) are below the literature range (0.206–0.220), and the difference between the obtained values and the lower range of literature values is 1.5% and 0.5%. The predicted mean drag coefficient values (0.94 and 0.97) remain within the range reported by previous experimental and LES investigations (0.94–1.04). Furthermore, only minor differences were

observed between the stationary-cylinder and overset mesh configurations. The relative difference between the Strouhal numbers was 1%, while the difference in the mean drag coefficient remained below 3.2%. These results indicate that the application of the overset mesh technique does not introduce significant numerical discrepancies. Therefore, the implemented numerical model was considered sufficiently validated for the prediction of aerodynamic wake dynamics in the subsequent analyses.

3.6. Simulation Results

The results were first presented in graphical form. The dynamic pressure distribution was selected as the most representative quantity for illustrating the obtained results. Figure 8 presents the wake flow structure formed behind the moving vehicle within the overset mesh region, including the recirculation zone and vortex formation associated with flow separation, as well as the dynamic pressure distribution during the vehicle pass-by event near the turbine.

Figure 8a presents the dynamic pressure distribution around the moving vehicle. The flow field is characterized by the formation of an unsteady aerodynamic wake downstream of the vehicle. Distinct vortex structures generated by flow separation can be observed behind the vehicle. The obtained flow behavior and wake structure are consistent with results reported in the literature [67,68]. Figure 8b presents the dynamic pressure distribution at the moment when the vehicle passes the turbine. The turbine is located within the turbulent wake region generated by the moving vehicle. Figure 8c presents streamlines in the vicinity of the turbine and the airflow guide vane. Recirculation zones and the complex flow behavior around the turbine blades and the guide vane are visible. The guide vane geometry partially directs the airflow toward the turbine blades and contributes to the separation of inflow and outflow streams within the turbine region.

As the key focus of the study is the energy recovery process, the principal criterion for evaluating each diffuser configuration is the amount of power generated by the turbine. To obtain the generated power values, the Report Definitions functionality in ANSYS Fluent was employed to extract the quantities required for power calculation. The turbine power output was calculated using Equation (8) [69].

$$P = \frac{V_{tan}}{r} \cdot T \tag{8}$$

where P—power [W], r—turbine radius [m], T—torque [N·m], V_{tan}—tangential velocity [m/s].

The torque was evaluated using the moment report function in ANSYS Fluent, with the moment calculated over the turbine blade surfaces. The angular velocity (ω) was obtained as the ratio of the tangential velocity at the turbine mesh interface to the radius of the turbine mesh domain.

For each of the four simulations, the instantaneous maximum power and the average turbine power were determined. The average turbine power was calculated by averaging the power signal over the interval beginning when the absolute value of turbine power exceeded 0.5 W, and ending when the absolute value dropped below 0.5 W and remained below this threshold for at least 0.5 s. An example of the generated power time history is presented in Figure 9. The function shown in Figure 9 begins at the moment when the turbine blades first intercept the airflow generated by the passing vehicle. This is immediately followed by a rapid increase in instantaneous power output. After the initial favorable impulse, the turbine power decreases to negative values. The occurrence of negative power values is attributed to the presence of highly turbulent airflow in the turbine region as well as to the variable aerodynamic loading conditions of the turbine and is a

commonly observed phenomenon in simulations of such processes [70,71]. Subsequently, the generated power oscillates between positive and negative values. After a short transient period, damping of the power oscillation amplitude is observed, followed by a gradual transition of the turbine to a stationary state.

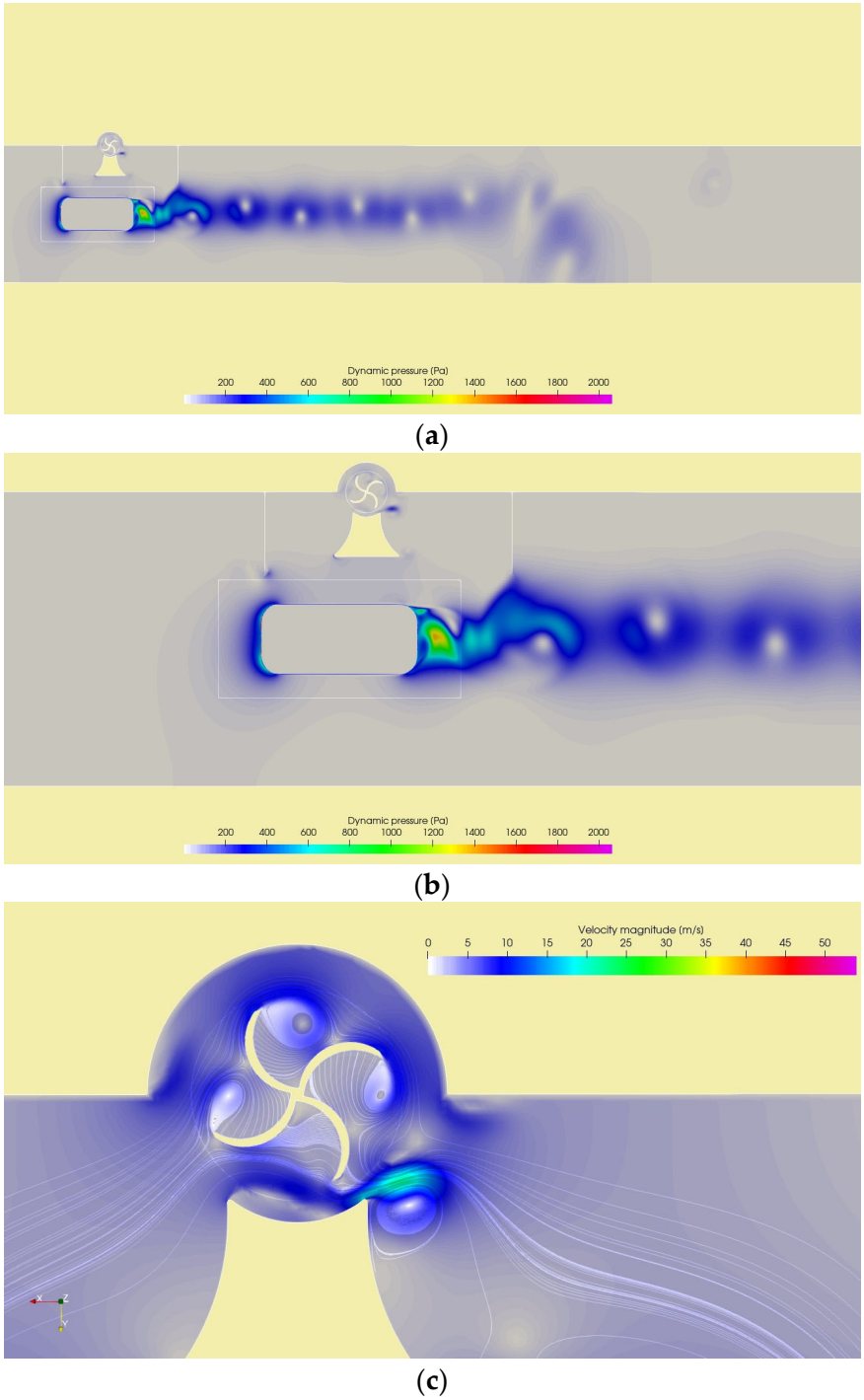

Figure 8. Dynamic pressure distribution for simulation with airflow guide vane configuration b (1.6 s of simulation): (**a**) vortex structures in the aerodynamic wake behind the vehicle; (**b**) pressure distribution during vehicle passage past the turbine; (**c**) streamlines in the turbine region.

The calculation results in the form of average and maximum instantaneous power values generated by the turbines are presented in Figure 10. The first conclusion is that the lowest average and maximum power values were obtained for the turbine operating without an airflow guide vane, which was consistent with expectations. The highest

average and peak instantaneous power values were achieved with deflector configuration b. The average power for this geometry is more than twice that obtained for deflector d and nearly four times higher than that of deflector c. It is also worth noting that configuration d exhibits a substantial difference between the maximum and average power values. This may be attributed to increased turbulence generated by this arrangement, leading to greater flow resistance and less stable turbine operation.

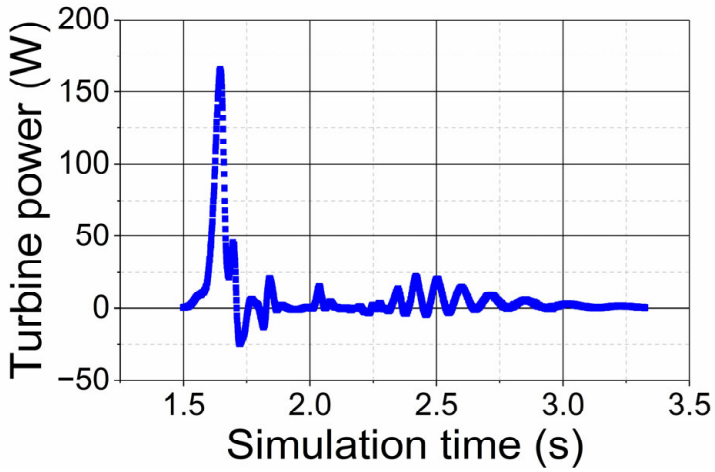

Figure 9. Time history of generated power for the simulation with the deflector configuration shown in Figure 3b.

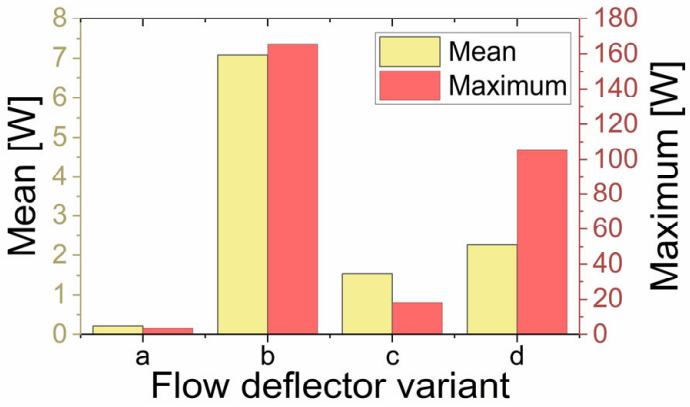

Figure 10. Average and maximum values of generated power.

3.7. Discussion of Results

The obtained turbine power values demonstrate that a single vehicle passing the turbine is capable of generating a measurable amount of energy despite the significant turbulence and flow non-uniformity observed both in the pressure field visualizations and in the recorded simulation parameters. The lowest power values were obtained for the case without an airflow guide vane, which is consistent with expectations. In the absence of a flow-directing structure, the kinetic energy of the airflow is dissipated before effectively reaching the turbine blades. The results obtained for deflector configuration c indicate excessive flow deceleration, resulting in insufficient utilization of the initial airflow impulse required to effectively accelerate the turbine. In contrast, configuration d exhibits the opposite behavior: a strong initial impulse provides effective turbine acceleration; however, the asymmetric diffuser geometry promotes the formation of additional turbulence, which rapidly decelerates the turbine. Consequently, despite the high instantaneous power peak, the average power value for this configuration remains only slightly higher than that of configuration c. The most effective design proved to be deflector configuration b. Both the

peak instantaneous power and the average generated power were significantly higher than those obtained for the remaining configurations. This was the only deflector specifically designed to promote rapid boundary layer separation from its surface, which enhances momentum transfer efficiency and enables effective acceleration of the turbine, in this case in the counterclockwise direction. The achieved average power of approximately 7 W per single vehicle pass in the vicinity of the turbine was considered a realistic value. These values, both average and maximum, are consistent with results reported in other studies conducted by researchers in similar configurations [51,56,57].

4. Conclusions

The conducted numerical analyses of three different airflow guide vane geometries, together with the baseline configuration without a flow guide, demonstrated the complexity of the investigated phenomenon. The obtained average recovered power of approximately 7 W during a single vehicle pass was considered a realistic value. The results confirm the potential of the proposed concept and provide a foundation for further research on roadside vehicle-induced energy harvesting systems.

However, the applied CFD model is subject to several limitations resulting from the adopted assumptions. The most significant limitation is the simplification of the analyzed geometry to a two-dimensional model. This assumption neglects certain three-dimensional flow phenomena, such as vortex structures generated in the wake of the vehicle, which may significantly influence the aerodynamic excitation and rotational behavior of the turbine. Consequently, the 2D approach may partially overestimate the obtained power output. Another important assumption concerns the application of the k–ε Enhanced Wall Treatment turbulence model. Although this model improves near-wall flow prediction, it may not fully capture highly unsteady vortex structures and transient turbulent interactions occurring in the wake region. Furthermore, the analyzed case was simplified by omitting several factors that could significantly influence the operation of the energy harvesting system. The vehicle model did not include detailed aerodynamic features and moved at a constant velocity. The turbine model also did not include the electromechanical conversion system, meaning that additional losses associated with generator efficiency and mechanical transmission were neglected. Moreover, the simulations were conducted without considering environmental conditions such as ambient wind, atmospheric disturbances, or varying traffic conditions. Another important limitation is the lack of experimental validation under laboratory or real-world conditions.

Despite these limitations, the numerical model successfully captured the qualitative relationships between vehicle-induced airflow and turbine performance, as well as the influence of flow-guide geometry on the energy recovery process. The observed differences between the analyzed configurations indicate that proper shaping of the airflow-guiding structures may substantially improve the effectiveness of roadside energy harvesting systems.

Future work may focus on extending the quantitative analysis by investigating a larger number of flow-guide geometries, as well as on conducting qualitative analyses using fully three-dimensional CFD models. Further studies should also include more complex traffic scenarios, such as multilane roads, multiple moving vehicles of different sizes, and interactions between several moving objects. An important next step would also be experimental validation, for example, using a closed-section wind tunnel, a dedicated outdoor test stand, or full-scale measurements performed on a closed road section or abandoned airfield. Validation methods may include Particle Image Velocimetry (PIV), Pitot tube measurements, or other velocity-field measurement techniques.

Author Contributions: Conceptualization, P.L.; methodology, P.L., M.P. and H.J.; software, M.P. and H.J.; validation, P.L., M.P. and H.J.; formal analysis, P.L., M.P. and H.J.; investigation, P.L., M.P. and H.J.; resources, P.L., M.P. and H.J.; data curation, M.P. and H.J.; writing—original draft preparation, P.L., M.P. and H.J.; writing—review and editing, P.L.; visualization, P.L., M.P. and H.J.; supervision, P.L.; project administration, P.L. All authors have read and agreed to the published version of the manuscript.

Funding: This research received no external funding.

Data Availability Statement: The original contributions presented in this study are included in the article. Further inquiries can be directed to the corresponding author.

Acknowledgments: This research was carried out with the support of the ANSYS National License coordinated by Interdisciplinary Centre for Mathematical and Computational Modeling University of Warsaw (ICM UW).

Conflicts of Interest: The authors declare no conflicts of interest.

Abbreviations

The following abbreviations are used in this manuscript:

CFD	Computational Fluid Dynamics
PIV	Particle Image Velocimetry
UDF	User-Defined Function
Six-DOF	Six Degrees of Freedom
HWA	Hot Wire Anemometer
LES	Large Eddy Simulation
FFT	Fast Fourier Transform

References

1. Lam, D. The next 2 billion: Can the world support 10 billion people? *Popul. Dev. Rev.* **2025**, *51*, 63–102.
2. Dora, B.K.; Bhat, S.; Mitra, A.; Ernst, D.; Halinka, A.; Zychma, D.; Sowa, P. The global electricity grid: A comprehensive review. *Energies* **2025**, *18*, 1152. [CrossRef]
3. Saxena, V. Water quality, air pollution, and climate change: Investigating the environmental impacts of industrialization and urbanization. *Water Air Soil Pollut.* **2025**, *236*, 73. [CrossRef]
4. Tran, B.L.; Tseng, W.C.; Chen, C.C. Climate change impacts on crop yields across temperature rise thresholds and climate zones. *Sci. Rep.* **2025**, *15*, 23424. [CrossRef] [PubMed]
5. Hirsch, Z.M.; Medgyesi, D.N.; Buresch, J.M.; Porter, J.R. A global multi-hazard framework for projecting climate migration flows to 2100 along shared socioeconomic pathways (SSPs). *Climate* **2026**, *14*, 81. [CrossRef]
6. Grünig, M.; Rammer, W.; Senf, C.; Albrich, K.; André, F.; Augustynczik, A.L.D.; Baumann, M.; Bohn, F.J.; Bouwman, M.; Bugmann, H.; et al. Climate change will increase forest disturbances in Europe throughout the 21st century. *Science* **2026**, *391*, eadx6329. [CrossRef] [PubMed]
7. Yang, S.; Fu, Y. Interconnectedness among supply chain disruptions, energy crisis, and oil market volatility on economic resilience. *Energy Econ.* **2025**, *143*, 108290. [CrossRef]
8. Wilk-Jakubowski, J.L.; Pawlik, L.; Wilk-Jakubowski, G.; Harabin, R. State-of-the-art in the use of renewable energy sources on the example of wind, wave energy, tidal energy, and energy harvesting: A review from 2015 to 2024. *Energies* **2025**, *18*, 1356. [CrossRef]
9. Jia, B.; Song, Z.; Li, X.; Hu, Z.; Li, Q. Enhancing Thermal Performance: The Evolution and Future of Solar Air Heaters with Baffles. *Case Stud. Therm. Eng.* **2025**, *75*, 107163. [CrossRef]
10. Ligęza, P. On search for unconventional energy sources for harvesting. *Energies* **2024**, *17*, 1091. [CrossRef]
11. Ligęza, P. Emergency Power Sources Operating Based on Energy Harvesting Processes for Application in Crisis Situations. *Energies* **2026**, *19*, 2263. [CrossRef]
12. Chye, W.C.; Dahari, Z.; Sidek, O.; Miskam, M.A. Electromagnetic micro power generator—A comprehensive survey. In Proceedings of the 2010 IEEE Symposium on Industrial Electronics and Applications (ISIEA), Penang, Malaysia, 3–5 October 2010; pp. 376–382. [CrossRef]
13. Gurusamy, N.; Elamvazuthi, I.; Yahya, N.; Su, S.; Truong, B.H. Simulation of electromagnetic generator as biomechanical energy harvester. *Appl. Sci.* **2022**, *12*, 6197. [CrossRef]

14. Parinov, I.A.; Cherpakov, A.V. Overview: State-of-the-art in the energy harvesting based on piezoelectric devices for last decade. *Symmetry* **2022**, *14*, 765. [CrossRef]
15. Covaci, C.; Gontean, A. Piezoelectric energy harvesting solutions: A review. *Sensors* **2020**, *20*, 3512. [CrossRef] [PubMed]
16. Peng, W.; Du, S. The advances in conversion techniques in triboelectric energy harvesting: A review. *IEEE Trans. Circuits Syst. I Regul. Pap.* **2023**, *70*, 3049–3062. [CrossRef]
17. Nguyen, Q.T.; Van Tam, T.; Vu, D.L.; Ahn, J.H.; Choi, W.M.; Ahn, K.K. Ultrahigh current density DC triboelectric generator for energy harvesting and self-powered sensing. *Nano Energy* **2025**, *143*, 111291. [CrossRef]
18. Zhao, L.C.; Zou, H.X.; Wu, Z.Y.; Gao, Q.H.; Yan, G.; Liu, F.R.; Wei, K.X.; Zhang, W.M. Dynamically Synergistic Regulation Mechanism for Rotation Energy Harvesting. *Mech. Syst. Signal Process.* **2022**, *169*, 108637. [CrossRef]
19. Zhao, L.C.; Zou, H.X.; Wei, K.X.; Zhou, S.X.; Meng, G.; Zhang, W.M. Mechanical Intelligent Energy Harvesting: From Methodology to Applications. *Adv. Energy Mater.* **2023**, *13*, 2300557. [CrossRef]
20. Zhao, L.C.; Chen, Z.W.; Gao, Q.H.; Wu, Z.Y.; Yan, G.; Wei, K.X.; Meng, G.; Zhang, W.M.; Zou, H.X. Self-Aligning Mechanism for Wearable Biomechanical Energy Harvesters. *Device* **2026**, *4*, 100972. [CrossRef]
21. He, J.; Li, K.; Jia, L.; Zhu, Y.; Zhang, H.; Linghu, J. Advances in the applications of thermoelectric generators. *Appl. Therm. Eng.* **2024**, *236*, 121813. [CrossRef]
22. Doraghi, Q.; Jouhara, H. Thermoelectric generator efficiency: An experimental and computational approach to analysing thermoelectric generator performance. *Therm. Sci. Eng. Prog.* **2024**, *55*, 102884. [CrossRef]
23. Zhou, Y.; Ho, G.W. Pyroelectric heat harvesting, what's next? *Next Energy* **2023**, *1*, 100026. [CrossRef]
24. Mohammadnia, A.; Rezania, A. Pyroelectric energy harvesting from power electronic substrates. *Energy Convers. Manag.* **2023**, *290*, 117233. [CrossRef]
25. Lazaroiu, A.C.; Gmal Osman, M.; Strejoiu, C.V.; Lazaroiu, G. A comprehensive overview of photovoltaic technologies and their efficiency for climate neutrality. *Sustainability* **2023**, *15*, 16297. [CrossRef]
26. Liu, X.; Sánchez-Sinencio, E. A highly efficient ultralow photovoltaic power harvesting system with MPPT for internet of things smart nodes. *IEEE Trans. Very Large Scale Integr. Syst.* **2015**, *23*, 3065–3075. [CrossRef]
27. Piñuela, M.; Mitcheson, P.D.; Lucyszyn, S. Ambient RF energy harvesting in urban and semi-urban environments. *IEEE Trans. Microw. Theory Tech.* **2013**, *61*, 2715–2726. [CrossRef]
28. Cansiz, M.; Altinel, D.; Kurt, G.K. Efficiency in RF energy harvesting systems: A comprehensive review. *Energy* **2019**, *174*, 292–309. [CrossRef]
29. Ligęza, P. Essential assessment of last-decade progress in road energy harvesting systems. *Energy Technol.* **2024**, *12*, 2301060. [CrossRef]
30. Su, B.; Guo, T.; Alam, M.M. A review of wind energy harvesting technology: Civil engineering resource, theory, optimization, and application. *Appl. Energy* **2025**, *389*, 125771. [CrossRef]
31. Páez-Montoro, A.; García-Valderas, M.; Olías-Ruíz, E.; López-Ongil, C. Solar energy harvesting to improve capabilities of wearable devices. *Sensors* **2022**, *22*, 3950. [CrossRef] [PubMed]
32. Al-Qadami, E.H.H.; Mustaffa, Z.; Al-Atroush, M.E. Evaluation of the pavement geothermal energy harvesting technologies towards sustainability and renewable energy. *Energies* **2022**, *15*, 1201. [CrossRef]
33. Ibrahim, H.H.; Singh, M.J.; Al-Bawri, S.S.; Ibrahim, S.K.; Islam, M.T.; Alzamil, A.; Islam, M.S. Radio frequency energy harvesting technologies: A comprehensive review on designing, methodologies, and potential applications. *Sensors* **2022**, *22*, 4144. [CrossRef] [PubMed]
34. Li, J.; Chen, N.; Yuan, X.; Wei, T. Hydraulic-based rotary electromagnetic energy harvester for road speed bumps. In Proceedings of the 2024 IEEE 2nd International Conference on Control, Electronics and Computer Technology (ICCECT), Jilin, China, 26–28 April 2024; pp. 493–497. [CrossRef]
35. Abdulwasea, A.; Liu, W. High-voltage speed bump design: Leveraging dual crank-shaft mechanisms for enhanced energy harvesting on road. *J. Mech. Sci. Technol.* **2025**, *39*, 3065–3077. [CrossRef]
36. Priyanka, D.; Gao, L. Advances in technologies for energy harvesting from pavements: A comprehensive review. *Appl. Sci.* **2026**, *16*, 3634. [CrossRef]
37. Shehu, L.; Yeon, J.H.; Song, Y. Piezoelectric energy harvesting for civil engineering applications. *Energies* **2024**, *17*, 4935. [CrossRef]
38. Qi, L.; Pan, H.; Bano, S.; Zhu, M.; Liu, J.; Zhang, Z.; Liu, Y.; Yuan, Y. A high-efficiency road energy harvester based on a chessboard sliding plate using semi-metal friction materials for self-powered applications in road traffic. *Energy Convers. Manag.* **2018**, *165*, 748–760. [CrossRef]
39. Fan, P.; Wang, D.; Zhang, Y.; Jiang, R.; Gu, H. An efficient traffic acoustic energy harvester using optimized Helmholtz resonators for sustainable roadside power generation and smart monitoring. *Energy Convers. Manag. X* **2025**, *28*, 101289. [CrossRef]
40. Yuan, M.; Cao, Z.; Luo, J.; Chou, X. Recent Developments of Acoustic Energy Harvesting: A Review. *Micromachines* **2019**, *10*, 48. [CrossRef] [PubMed]

41. Ligęza, P.; Jamróz, P.; Socha, K. Development trends of air flow velocity measurement methods and devices in renewable energy. *Energies* **2025**, *18*, 412. [CrossRef]
42. Cai, C.; Ming, T.; Fang, W.; De Richter, R.; Peng, C. The effect of turbulence induced by different kinds of moving vehicles in street canyons. *Sustain. Cities Soc.* **2020**, *54*, 102015. [CrossRef]
43. Ligęza, P.; Jamróz, P. A hot-wire anemometer with automatically adjusted dynamic properties for wind energy spectrum analysis. *Energies* **2022**, *15*, 4618. [CrossRef]
44. Tian, W.; Mao, Z.; Li, Y. Numerical simulations of a VAWT in the wake of a moving car. *Energies* **2017**, *10*, 478. [CrossRef]
45. Liew, H.F.; Baharuddin, I.; Rosemizi, A.R.; Muzamir, I.; Hassan, S.I.S. Review of feasibility wind turbine technologies for highways energy harvesting. *J. Phys. Conf. Ser.* **2020**, *1432*, 012059. [CrossRef]
46. Rana, S.; Roy, B.; Saha, B.B.; Ghosh, S. Energy harvesting from highway traffic vehicles movement via VAWT. *Sciences (IEICES)* **2022**, *8*, 122–127. [CrossRef]
47. Sharma, N.; Wan, X.; Duan, Z.; Xiao, X.; Yin, J.; Du, Y.; Chen, J. Harvesting low-grade wind energy from highways using a triboelectric nanogenerator. *Nano Energy* **2024**, *132*, 110354. [CrossRef] [PubMed]
48. Muyambo, R.D.; Muhla, T.; Kanyemba, G.; Mashava, D.; Munhuwamambo, G.; Mapindu, I. Design and development of a vertical axis wind turbine for slip stream energy harvesting. *Glob. J. Eng. Technol. Adv.* **2025**, *23*, 10–20. [CrossRef]
49. ANSYS Inc. *Ansys Fluent Theory Guide*; ANSYS Inc.: Canonsburg, PA, USA, 2026.
50. Launder, B.E.; Spalding, D.B. The numerical computation of turbulent flows. *Comput. Methods Appl. Mech. Eng.* **1974**, *3*, 269–289. [CrossRef]
51. Duc, L.; Phan, T.D.; Jufar, S. Effects of Car Wake on Performance of Low-Capacity Wind Turbine Mounted on Highways. In Proceedings of the International Exchange and Innovation Conference on Engineering & Sciences (IEICES), Fukuoka, Japan, 28–30 October 2023; Volume 9, pp. 188–195. [CrossRef]
52. Mazlan, M.Z.; Mohd Zawawi, F.; Tahzib, T.; Ismail, K.; Samion, S. Performance Analysis of Highway Wind Turbine Enhanced with Wind Guide Vanes Using the Taguchi Method. *CFD Lett.* **2021**, *13*, 25–42. [CrossRef]
53. Sadegh Toudarbari, M.J.; Maghrebi, M.J.; Hashemzadeh, A. Evaluation of Darrieus Wind Turbine for Different Highway Settings Using CFD Simulation. *Sustain. Energy Technol. Assess.* **2021**, *45*, 101077. [CrossRef]
54. Katz, A.; Sankaran, V. Mesh quality effects on the accuracy of CFD solutions on unstructured meshes. *J. Comput. Phys.* **2011**, *230*, 7670–7686. [CrossRef]
55. Ferziger, J.H.; Perić, M. *Computational Methods for Fluid Dynamics*, 3rd ed.; Springer: Berlin, Germany, 2002.
56. Ulus, A.; Moldovan, S.I. Optimization of Vertical Axis Wind Turbine Systems to Capture Vehicle-Induced Highway Winds. *Energies* **2025**, *18*, 3139. [CrossRef]
57. Tian, W.; Song, B.; Mao, Z. Numerical Investigation of Wind Turbines and Turbine Arrays on Highways. *Renew. Energy* **2020**, *147*, 384–398. [CrossRef]
58. Available online: https://www.grc.nasa.gov/www/k-12/VirtualAero/BottleRocket/airplane/dragco.html (accessed on 9 June 2026).
59. Available online: https://www.sciencedirect.com/topics/physics-and-astronomy/strouhal-number (accessed on 9 June 2026).
60. Parnaudeau, P.; Carlier, J.; Heitz, D.; Lamballais, E. Experimental and Numerical Studies of the Flow over a Circular Cylinder at Reynolds Number 3900. *Phys. Fluids* **2008**, *20*, 085101. [CrossRef]
61. Kravchenko, A.G.; Moin, P. Numerical Studies of Flow over a Circular Cylinder at ReD = 3900. *Phys. Fluids* **2000**, *12*, 403–417. [CrossRef]
62. Lysenko, D.A.; Ertesvåg, I.S.; Rian, K.E. Large-Eddy Simulation of the Flow over a Circular Cylinder at Reynolds Number 3900 Using the OpenFOAM Toolbox. *Flow Turbul. Combust.* **2012**, *89*, 491–518. [CrossRef]
63. Ouvrard, H.; Koobus, B.; Dervieux, A.; Salvetti, M.V. Classical and Variational Multiscale LES of the Flow around a Circular Cylinder on Unstructured Grids. *Comput. Fluids* **2010**, *39*, 1083–1094. [CrossRef]
64. Lourenco, L.M.; Shih, C. Characteristics of the Plane Turbulent Near Wake of a Circular Cylinder: A Particle Image Velocimetry Study. 1993; *unpublished*.
65. Mani, A.; Moin, P.; Wang, M. Computational Study of Optical Distortions by Separated Shear Layers and Turbulent Wakes. *J. Fluid Mech.* **2009**, *625*, 273–298. [CrossRef]
66. Franke, J.; Frank, W. Large Eddy Simulation of the Flow Past a Circular Cylinder at Re = 3900. *J. Wind Eng. Ind. Aerodyn.* **2002**, *90*, 1191–1206. [CrossRef]
67. Li, R.; Soper, D.; Xu, J.; Jia, Y.; Niu, J.; Hemida, H. A separated-flow model for 2-D viscous flows around bluff bodies using the panel method. *Appl. Sci.* **2022**, *12*, 9652. [CrossRef]
68. Alvarez, A.J.; Nieto, F.; Kwok, K.K.C.S.; Hernandez, S. A simplified CFD approach for bluff-body aerodynamics under small scale free stream turbulent flow. *J. Wind Eng. Ind. Aerodyn.* **2023**, *241*, 105500. [CrossRef]
69. Velichkova, R.; Iliev, R.; Pichurov, G.; Markov, D.; Simova, I.; Pushkarov, M.; Tsalov, T. Numerical study of the torque and power of a hydraulic turbine with oscillating blades. *Energies* **2023**, *16*, 6744. [CrossRef]

70. Kyle, R.; Früh, W.-G. The transitional states of a floating wind turbine during high levels of surge. *Renew. Energy* **2022**, *200*, 1469–1489. [CrossRef]
71. Maher, N.S.; Ghazalla, R.A.; Mohamed, M.H.; Nawar, M.A.A.; Attai, Y.A. An innovative approach for harnessing wind power by Darrieus turbines using a passive flow controller. *J. Eng. Appl. Sci.* **2025**, *72*, 56. [CrossRef]